Rational construction of a library of M_{29} nanoclusters from monometallic to tetrametallic

Xi Kang[a], Xiao Wei[a], Shan Jin[a], Qianqin Yuan[a], Xinqi Luan[b], Yong Pei[b], Shuxin Wang[a,1], Manzhou Zhu[a,1], and Rongchao Jin[c,1]

[a]Department of Chemistry and Centre for Atomic Engineering of Advanced Materials, Anhui Province Key Laboratory of Chemistry for Inorganic/Organic Hybrid Functionalized Materials, Anhui University, 230601 Hefei, Anhui, China; [b]Department of Chemistry, Key Laboratory of Environmentally Friendly Chemistry and Applications of Ministry of Education, Xiangtan University, 411105 Xiangtan, Hunan, China; and [c]Department of Chemistry, Carnegie Mellon University, Pittsburgh, PA 15213

Exploring intermetallic synergy has allowed a series of alloy nanoparticles with prominent chemical–physical properties to be produced. However, precise alloying based on a maintained template has long been a challenging pursuit, and little has been achieved for manipulation at the atomic level. Here, a nanosystem based on $M_{29}(S\text{-}Adm)_{18}(PPh_3)_4$ (where S-Adm is the adamantane mercaptan and M is Ag/Cu/Au/Pt/Pd) has been established, which leads to the atomically precise operation on each site in this M_{29} template. Specifically, a library of 21 species of nanoclusters ranging from monometallic to tetrametallic constitutions has been successfully prepared step by step with in situ synthesis, target metal-exchange, and forced metal-exchange methods. More importantly, owing to the monodispersity of each nanocluster in this M_{29} library, the synergetic effects on the optical properties and stability have been mapped out. This nanocluster methodology not only provides fundamental principles to produce alloy nanoclusters with multimetallic compositions and monodispersed dopants but also provides an intriguing nanomodel that enables us to grasp the intermetallic synergy at the atomic level.

nanocluster | alloy | intermetallic synergy | photoluminescence

It has been *ca*. 5,000 y since the Bronze Age in which "alloying" was first practiced. Alloying has indeed become the most important strategy in tailoring the physical/chemical performances of metal materials. In recent decades, colloidal nanoparticles have been of tremendous academic and industrial interest due to their extraordinary catalytic, optical, magnetic, and electrochemical properties, because alloying of metal nanoparticles with heterometals has proven to be a versatile strategy for improving the nanoparticle performances (1–5). In general, owing to the synergistic effect, alloys often display enhanced properties relative to the monometallic homologs, which largely broadens the applications of such nanomaterials (1–5). However, a detailed understanding of how the synergistic effect arises remains elusive for 2 main reasons: 1) nanoparticles that are uniform at the atomic level are difficult to prepare (usually, a distribution of size was obtained) and 2) their surface chemistry (e.g., metal–ligand interactions) is difficult to study (6). Nanochemists are often frustrated by the well-known fact that no 2 nanoparticles are the same, which precludes the fundamental study on many properties of colloidal nanoparticles in which the total structures must be known. Besides, the atomic-level tailoring of specific sites of nanoparticles with specific numbers of heterometals remains so far the least feasible. Atomic-level understanding of the synergism and atomically precise control over alloy compositions require precise molecular entities to serve as model nanosystems and precise molecular tools.

Atomically precise metal nanoclusters with ultrasmall sizes (e.g., <2-nm diameter of the metallic core) provide an exciting opportunity for investigating structure–property correlations at the atomic level, owing to their uniform size and precise structure (6–23). The quantum size effects of nanoclusters also lead to

unprecedented intermetallic quantum synergisms (24–34), and such knowledge will serve as the key to fine tailoring of the physical/chemical performances of alloy nanoparticles. As to the composition/structure of alloy nanoclusters, due to the differences in size and electronegativity each type of heteroatom may prefer different site(s) in the parent nanocluster (35, 36). Taking the most researched $Au_{25}(SR)_{18}$ as an example, the Ag dopants are preferentially doped at the icosahedral shell, whereas the Cu dopants go to the staple motifs, albeit Cu and Ag are in the same group of gold (37, 38). By comparison, a single Pt or Pd heteroatom can be doped in the Au_{25} nanocluster template, namely $M_1Au_{24}(SR)_{18}$, wherein the Pt or Pd dopant occupies the central position (39, 40). However, monodispersity of the dopants such as Ag and Cu remains extremely challenging in the $M_xAu_{25-x}(SR)_{18}$ (where x is often a range of Ag or Cu heteroatoms), and this phenomenon extends to other cluster templates. The attainment of monodispersity (i.e., x being a definite number, rather than a range) from bimetallic to multimetallic nanoclusters with the preserved structure is highly desirable for revealing the precise composition–property correlations, and such correlations

Significance

Precise alloying in nanoparticles with the structure retained has long been a major challenge. In addition, little has been achieved for alloy manipulation at the atomic level. Although several structures of bimetallic nanoclusters have been reported, the monodispersity of dopants remains challenging, not to mention the tri- or multimetallic nanoclusters. Here we present a maneuverable nanosystem based on an M_{29} (M = Au/Ag/Pt/Pd/Cu) nanocluster with the tetra-stratified configuration $M_1(center)@M_{12}(first shell)@M_{12}(SR)_{18}(second shell)@(M\text{-}PPh_3)_4(vertex)$. A rich library of 21 nanoclusters ranging from monometallic to tetrametallic compositions has been rationally constructed. The synergetic effects on optical properties and stability have been explicitly mapped out. Our methodology provides fundamental principles toward controllable alloying at the nanoscale with multimetallic compositions and atomically monodispersed dopants.

will allow the controllable syntheses of new alloy nanomaterials with novel structure/composition and tailored performance.

In this work, we exploit the nanocluster system $M_{29}(S\text{-}Adm)_{18}(PPh_3)_4$ (where M = Ag/Au/Cu/Pt/Pd and S-Adm is adamantanethiolate) to prepare a rich library of multimetallic nanoclusters, with which the atomic-level tailoring has been accomplished in terms of the doping sites, the heterometal types, and the alloying contents. The M_{29} template possesses a tetra-stratified configuration: $M(center)@M_{12}(first\ shell)@M_{12}(SR)_{18}(second\ shell)@(Ag\text{-}PPh_3)_4(vertex)$. In particular, owing to the accessibility of each site with multichoices of metals, a rich library of 21 species of nanoclusters ranging from monometallic to tetrametallic compositions has been successfully prepared step by step via the combination of the in situ synthesis, the targeted metal exchange, and the forced metal exchange. The atomic monodispersity of each nanocluster in this M_{29} library has been characterized by electrospray ionization mass spectrometry (ESI-MS) analysis. Among them, $Pt_1Ag_{12}Cu_{12}Au_4(SR)_{18}(PPh_3)_4$ and $Pd_1Ag_{12}Cu_{12}Au_4(SR)_{18}(PPh_3)_4$ are tetrametallic nanoclusters with atomic monodispersity. More importantly, the optical properties and thermal stability of these M_{29} nanoclusters have been compared, and the synergetic effects on these properties have been mapped out at the atomic level. Overall, this M_{29} (M = Ag/Au/Cu/Pt/Pd) nanosystem offers an ideal platform for unprecedented systematic evaluation of the synergistic effects, which provides impetus for future experimental and theoretical developments on controllable alloy nanomaterials with enhanced performance.

Results and Discussion

The M_{29} Alloy Library. A nanocluster methodology involving a stepwise approach (in situ synthesis–targeted metal exchange–forced metal exchange) has been exploited to alloy the monometallic Ag_{29} nanocluster with different metals and to form a rich library of multimetallic nanoclusters with a unified configuration as $M_1(kernel)@M_{12}(first\ shell)@M_{12}(SR)_{18}(second\ shell)@(M\text{-}PPh_3)_4(vertex)$ (M = Ag/Au/Pd/Pt/Cu) (Fig. 1). Specifically, bimetallic $M_1Ag_{28}(SR)_{18}(PPh_3)_4$ (M = Au/Pt/Pd) nanoclusters are all composed of 28 silver atoms and a single heteroatom. From each bimetallic M_1Ag_{28} nanocluster, 4 trimetallic nanoclusters with different second-shell@vertex compositions have been prepared, for example from Pt_1Ag_{28} to $Pt_1Ag_{24}Cu_4$, $Pt_1Ag_{24}Au_4$, $Pt_1Ag_{12}Cu_{16}$, and $Pt_1Ag_{16}Cu_{12}$. Note that the central-Pt/Pd/Au atom as well as the Ag_{12} first shell in such bimetallic nanoclusters is retained in the subsequent alloying processes. Furthermore, the Au-doping operation (i.e., the forced metal-exchange method, discussed below) on the $(Pt/Pd)_1Ag_{12}Cu_{16}$

trimetallic nanoclusters creates the corresponding tetrametallic nanoclusters that follow an arrangement of tetra-stratified Pt/Pd (center)@Ag_{12}(first shell)@$Cu_{12}(SR)_{18}$(second shell)@$(AuPPh_3)_4$ (vertex). Each nanocluster (except Pt/Pd doping) adopts a "+3" charge state, while the M_{29} nanoclusters containing a single Pt or Pd heteroatom are in a "+2" charge state. Since the central Pt/Pd atom contributes no free valence electron, the nominal electron count of each nanocluster in this M_{29} library is 8e.

Controlling the Central Atom in the M_{29} Template. The parent Ag_{29} and single-heteroatom doped M_1Ag_{28} (M = Au/Pt/Pd) nanoclusters have been successfully prepared via an in situ synthetic procedure. The optical absorption, emission, and ESI-MS results of the obtained Pt_1Ag_{28} are the same as those reported previously (41), where the single-Pt atom occupies the innermost center of the face-centered (fcc) Pt_1Ag_{12} core (Fig. 2; also see *SI Appendix*, Fig. S1 for the structural anatomy of the M_1Ag_{28} nanoclusters). Similarly, the central occupation of the single heteroatom has been observed in the crystal structure of $Au_1Ag_{28}(SR)_{18}(PPh_3)_4$. Considering 1) the homolog of these $M_1Ag_{28}(SR)_{18}(PPh_3)_4$ nanoclusters, 2) the central occupying tendency of the Pd heteroatom in the M_{13} kernel (25, 40), and 3) the same Pd X-ray photoelectron spectroscopy (XPS) signal between $Pd_1Ag_{28}(SR)_{18}(PPh_3)_4$ and $Pd_1Ag_{24}(S\text{-}PhMe_2)_{18}$ (*SI Appendix*, Fig. S2), we thus propose the similar construction of the Pd_1Ag_{28} with the determined structures of Pt_1Ag_{28} and Au_1Ag_{28} nanoclusters. In the fcc M_1Ag_{12} core, the coordination number of the innermost metal is 12, the same as that in the fcc crystal lattice of the bulk Au/Ag/Pt/Pt or their alloys.

ESI-MS was performed to validate the monodispersity of each nanocluster (Fig. 2, *Bottom*). First of all, the ESI-MS of each purified product shows a single intense peak, demonstrating the monodispersity of each nanocluster. In addition, the spacing of the mass peaks indicates a "3+" charge state of Ag_{29} and Au_1Ag_{28} nanoclusters but a "2+" charge state for the single Pt or Pd-doped M_1Ag_{28}, indicating no free valence electron contribution from the Pt or Pd dopant. Accordingly, these 4 nanoclusters all represent an 8-electron closed-shell electronic configuration (i.e., 29-18-3 = 8e for Ag_{29} and Au_1Ag_{28} and 28-18-2 = 8e for Pt_1Ag_{28} and Pd_1Ag_{28}).

Controlling the Shell Atoms in the M_{29} Template. Transforming the M-Ag (M = Au/Pt/Pd) "precursor" into the M-Ag-Cu results in the generation of trimetallic $M_1Ag_{16-x}Cu_{12+x}$ nanoclusters with polydispersed x = 0–4. Considering that the number of the alternative occupying sites (i.e., 4) is the same as that of the
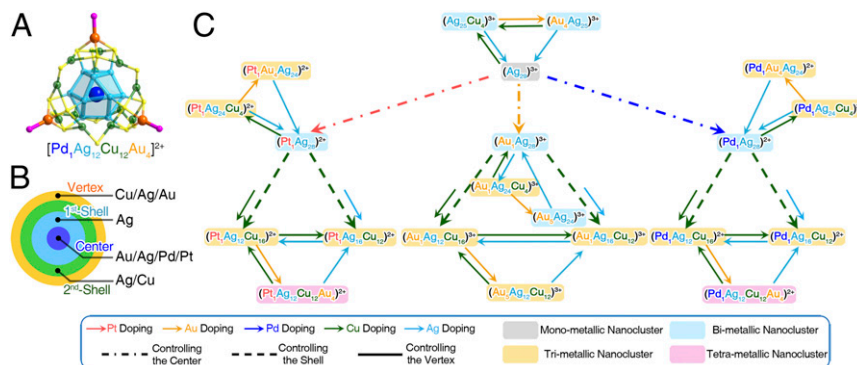
Fig. 1. The library of M_{29} nanoclusters. (*A*) Structure of the tetrametallic $Pd_1Ag_{12}Cu_{12}Au_4(S\text{-}Adm)_{18}(PPh_3)_4$ nanocluster. (*B*) Structural anatomy of the center, first shell, second shell, and vertex. (*C*) Schematic illustration of the stepwise alloying process from monometallic to bi-, tri-, and tetrametallic nanoclusters on the basis of the M_{29} template. The pink, orange, blue, green, and cerulean arrows indicate the alloying pathways of doping Pt, Au, Pd, Cu, and Ag, respectively. The gray, blue, orange, and purple backgrounds indicate the mono-, bi-, tri-, and tetrametallic compositions of each nanocluster, respectively. For clarity, the ligand parts (SR and PPh_3) are omitted in labels (the same below).

Fig. 2. M_{29} nanoclusters from monometallic to bimetallic. Structures and ESI-MS spectra of (*A*) Ag_{29} and its central doped (*B*) Au_1Ag_{28}, (*C*) Pt_1Ag_{28}, and (*D*) Pd_1Ag_{28} nanoclu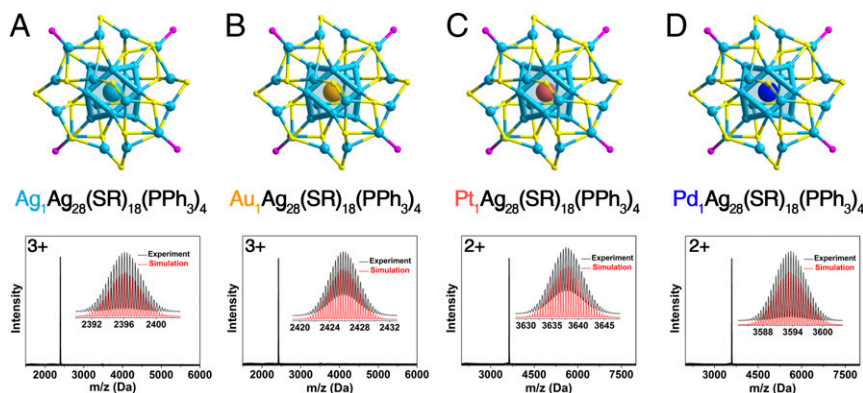sters. (*Insets*) Experimental and simulated isotope patterns of each nanocluster. Color codes: cerulean sphere, Ag; orange sphere, Au; pink sphere, Pt; blue sphere, Pd; yellow sphere, S; purple sphere, P. For clarity, the carbon and hydrogen atoms are not shown.

vertex Ag-PPh$_3$ units in the Ag$_{29}$ template, these vertex sites are proposed to be the Ag-to-Cu exchange locations; in other words, the Ag$_{12}$(first shell)@Cu$_{12}$(second shell) constructions in such nanoclusters are nonswappable. Density functional theory (DFT) calculations also demonstrated that the metal-exchange location is the vertex, instead of sites on the second shell (*SI Appendix*, Figs. S3 and S4). Besides, by summing up the previous alloy nanoclusters that containing the Au/Ag and Cu metals (42–44), it is suggested that the first shell in this M_{29} template is totally occupied by the 12 Ag atoms, and the second-shell metal is Cu (such arrangements have also been confirmed by the crystal structure of Pt$_1$Ag$_{12}$Cu$_{16}$(SR)$_{18}$(PPh$_3$)$_4$). Taking the Pt-centered nanosystem as an example (Fig. 3, *Left*), the ESI-MS spectrum of the in situ-prepared product displays 5 peaks centered at 3283.3, 3305.3, 3327.3, 3349.8, and 3371.8 Da, corresponding to the Pt$_1$Ag$_{12}$Cu$_{16}$(SR)$_{18}$(PPh$_3$)$_4$, Pt$_1$Ag$_{13}$Cu$_{15}$(SR)$_{18}$(PPh$_3$)$_4$, Pt$_1$Ag$_{14}$Cu$_{14}$(SR)$_{18}$(PPh$_3$)$_4$, Pt$_1$Ag$_{15}$Cu$_{13}$(SR)$_{18}$(PPh$_3$)$_4$, and Pt$_1$Ag$_{16}$Cu$_{12}$(SR)$_{18}$(PPh$_3$)$_4$, respectively (*SI Appendix*, Figs. S5 and S6). The mass spacing of adjacent peaks is 22 Da, which matches the expected gap between Ag and Cu atoms, that is, [M(Ag)-M(Cu)]/2(charge) = 22 Da. Consequently, the trimetallic Pt@Ag@Cu

nanoclusters have been successfully synthesized, albeit with polydispersed dopant numbers (Fig. 3, *Left*).

The metal-exchange method has been extensively exploited to alloy the parent nanocluster with a retained framework (28, 35, 36). For example, the icosahedral-shell Au atoms are substituted by Ag atoms when alloying Au$_{25}$(SR)$_{18}$ with the Ag^I-SR complex (35). Besides, the reversible process has been observed by reacting the as-alloyed Ag$_x$Au$_{25-x}$(SR)$_{18}$ with the Au^I–SR complex (35). In this context, we are motivated to "focus" the distribution of Pt$_1$Ag$_{16-x}$Cu$_{12+x}$(SR)$_{18}$(PPh$_3$)$_4$ into monodispersed nanoclusters (i.e., a single x value) by way of a targeted metal-exchange method. As depicted in Fig. 3, we indeed found that reaction of the Pt$_1$Ag$_{16-x}$Cu$_{12+x}$(SR)$_{18}$(PPh$_3$)$_4$ with a large amount of Ag^I(PPh$_3$)NO$_3$ complex generates the monodispersed Pt$_1$Ag$_{16}$Cu$_{12}$(SR)$_{18}$(PPh$_3$)$_4$ nanocluster, which exhibits a single mass peak centered at 3,371.8 Da in the ESI-MS spectrum. Accordingly, the substitution of vertex Cu atoms by Ag atoms occurs in the parent nanoclusters. Furthermore, the detected [Cu^I(PPh$_3$)$_2$]$^+$ (centered at 587.11 Da; *SI Appendix*, Fig. S7; ESI-MS spectra of the starting Pt$_1$Ag$_{16-x}$Cu$_{12+x}$(SR)$_{18}$(PPh$_3$)$_4$ are shown in *SI Appendix*, Figs. S5 and S6) also validates the targeted metal-exchange process, which can be summarized as
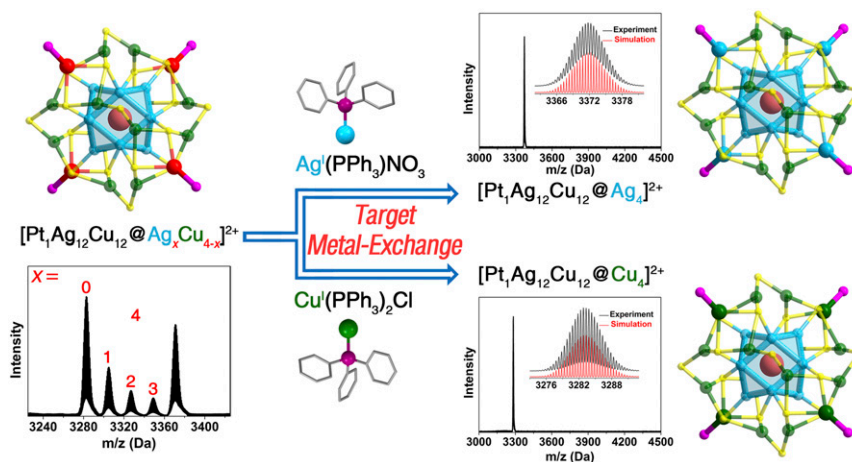

Fig. 3. M_{29} nanoclusters with trimetallic compositions. Structures and ESI-MS spectra of Pt$_1$Ag$_{12}$Cu$_{12}$@Ag$_x$Cu$_{4-x}$(SR)$_{18}$(PPh$_3$)$_4$ (x = 0–4) and its metal-exchanged products: trimetallic Pt$_1$Ag$_{16}$Cu$_{12}$(SR)$_{18}$(PPh$_3$)$_4$ and Pt$_1$Ag$_{12}$Cu$_{16}$(SR)$_{18}$(PPh$_3$)$_4$ nanoclusters with monodispersity. (*Insets*) Experimental and simulated isotope patterns of each nanocluster. Color codes: cerulean sphere, Ag; pink sphere, Pt; green sphere, Cu; red sphere, mixed Ag/Cu; yellow sphere, S; purple sphere, P. Carbon and hydrogen atoms are not shown. For clarity, the chemical formula of each nanocluster is only marked with the corresponding metal composition (the same below), because all nanoclusters in this M_{29} system follow the same configuration as M$_1$@M$_{12}$@M$_{12}$(SR)$_{18}$@(M-PPh$_3$)$_4$ (M = Ag/Au/Pd/Pt/Cu).

www.manaraa.com

$$Pt_1Ag_{12}Cu_{12}(SR)_{18}@Ag_xCu_{4-x}(PPh_3)_4 + (4-x)\ Ag^I(PPh_3)NO_3$$
$$\rightarrow Pt_1Ag_1Cu_{12}(SR)_{18}@Ag_4(PPh_3)_4 + (4-x)\ Cu^I(PPh_3)_2NO_3.$$
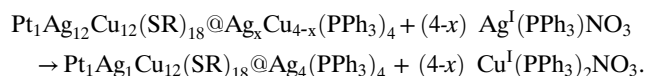
On the other hand, reacting the $Pt_1Ag_{16-x}Cu_{12+x}(SR)_{18}(PPh_3)_4$ with $Cu^I(PPh_3)_2Cl$ results in the monodispersed $Pt_1Ag_{12}Cu_{16}(SR)_{18}(PPh_3)_4$ nanocluster, whose composition and construction have been verified by the ESI-MS analysis and X-ray crystallography (Fig. 3, *Lower Right* and *SI Appendix*, Fig. S8). Besides, Pd-centered and Au-centered trimetallic nanoclusters have also been obtained with a procedure similar to that of the Pt-centered nanosystem (see *SI Appendix*, Figs. S9–S13 for the Pd-centered nanosystem and *SI Appendix*, Figs. S14–S18 for the Au-centered nanosystem).

Controlling the Vertex Atoms in the M$_{29}$ Template. Based on the above understandings of the vertex metal atoms (bonded with the PPh$_3$ ligands) with exchangeable characteristic, we perceive a good opportunity to obtain the alloyed M$_{29}$ nanoclusters containing more than 3 types of metals. Recently, Negishi and coworkers (36) reported the synthesis of tetrametallic $Pd_1Ag_xCu_yAu_{24-x-y}(SR)_{18}$ nanoclusters by exploiting the metal-exchange rules that different metal dopants preferentially occupy different sites in the parent $Au_{25}(SR)_{18}$ nanocluster. However, alloying in the Au_{25} template always results in a mixture product with distributed dopant numbers, for example Ag_xAu_{25-x} and Cu_xAu_{25-x} nanoclusters (35, 37, 38). In comparison, the M$_{29}$ nanosystem can act as a perfect model to obtain the multimetallic nanocluster in atomic monodispersity. As shown in Fig. 4 and *SI Appendix*, Figs. S19 and S20, the further metal-exchange operation on the trimetallic $Pt_1Ag_{12}Cu_{16}(SR)_{18}(PPh_3)_4$ has been performed by reacting the nanocluster with $Au^I(PPh_3)Cl$. On the one hand, the alloying outcomes follow an incompletely metal-exchanged pattern [even with the overdose of $Au^I(PPh_3)Cl$] and 5 peaks including $Pt_1Ag_{12}Cu_{12}@Cu_4(SR)_{18}(PPh_3)_4$, $Pt_1Ag_{12}Cu_{12}@Cu_3Au_1(SR)_{18}(PPh_3)_4$, $Pt_1Ag_{12}Cu_{12}@Cu_2Au_2(SR)_{18}(PPh_3)_4$, $Pt_1Ag_{12}Cu_{12}@Cu_1Au_3(SR)_{18}(PPh_3)_4$, and $Pt_1Ag_{12}Cu_{12}@Au_4(SR)_{18}(PPh_3)_4$ are detected in the ESI-MS (note that the maximum Au alloying number is 4, validating the vertex alloying mode in these M$_{29}$ nanosystems). On the other hand, reacting the mixture of $Pt_1Ag_{12}Cu_{16-x}Au_x(SR)_{18}(PPh_3)_4$ ($x = 0$–4) nanoclusters with only tiny amounts of $Cu^I(PPh_3)_2Cl$ results in the monodispersed $Pt_1Ag_{12}Cu_{16}(SR)_{18}(PPh_3)_4$ nanocluster (Fig. 4). Combining the above 2 aspects, it is suggested that the bonding ability of Cu atoms in these 4 vertex sites is far stronger than that of the Au atoms. Considering that 1) the bonding mode of these vertex metals is μ$_3$-M (M = Cu/Au) and 2) μ$_3$-Cu has been reported

several times (however, μ$_3$-Au has not been observed yet) (42–44), we speculate that the stability of such μ$_3$-Au is not as high as that of the μ$_3$-Cu in the M$_{29}$ nanosystem (*SI Appendix*, Fig. S21). The instability of vertex-Au nanoclusters has also been proved by the stability tests (discussed below) as well as DFT calculations (*SI Appendix*, Fig. S3).

For obtaining the tetrametallic $Pt_1Ag_{12}Cu_{12}Au_4$ nanocluster with monodispersity, the 4 vertex Cu atoms should be substituted by the Au dopants completely. By analyzing the ESI-MS results of metal-exchange processes from $Pt_1Ag_{16-x}Cu_{12+x}$ to $Pt_1Ag_{12}Cu_{16}$ (or $Pt_1Ag_{16}Cu_{12}$), no oxidation-reduction but just metal-exchange processes Ag(I)→Cu(I) or Cu(I)→Ag(I) occur, indicating that the vertex Cu atoms are almost in the Cu(I) valence state. By noting that adding the $Cu^{II}(PPh_3)_2Cl_2$ to the $Pt_1Ag_{16-x}Cu_{12+x}$ nanoclusters cannot convert them into monodispersed $Pt_1Ag_{12}Cu_{16}$ (*SI Appendix*, Fig. S22), we hypothesize that the Cu(II) atoms have no coordination ability to act as the μ$_3$-Cu at the vertex sites. Therefore, considering the competitive relationship of Au and Cu in these sites, the oxidation capability of H_2O_2 has been exploited to weaken the coordination ability of Cu atoms and this indeed allows us to prepare the monodispersed $Pt_1Ag_{12}Cu_{12}Au_4$ nanocluster (Fig. 4, *Right*). In this "forced metal-exchange" process, the addition of H_2O_2 turns the Cu(I) into the oxidized state [Cu(II), shown in *SI Appendix*, Fig. S23], and further addition of the $Au^I(PPh_3)Cl$ guarantees the existence of the Au(I) that is able to occupy the vertex sites. The $H_2O_2/Au^I(PPh_3)Cl$ addition is repeated 3 times to eliminate the Cu^I coordination completely, and then ESI-MS demonstrates the generation of the tetrametallic $Pt_1Ag_{12}Cu_{12}Au_4(SR)_{18}(PPh_3)_4$ with monodispersity (the Pd-centered procedure and results are in *SI Appendix*, Figs. S24–S26). This result is exciting since it not only produces a tetrametallic nanocluster with precise metallic occupancy but also evokes the possibility for revealing the intermetallic synergy in detail in a coherent monodispersed nanosystem from monometallic to bi-, tri-, and tetrametallic compositions. However, the obtained Au-vertex nanoclusters ($Pt_1Ag_{12}Cu_{12}Au_4$ or $Pd_1Ag_{12}Cu_{12}Au_4$) are less stable and decompose in solution (*SI Appendix*, Fig. S23), in agreement with the DFT results that the energy of Au-vertex nanoclusters is much higher than that of Cu-vertex nanoclusters (*SI Appendix*, Fig. S3).

Overview of the Unique M$_{29}$ Nanosystem. As summarized in *SI Appendix*, Fig. S27, a unique nanosystem has been established based on the Pt-centered M$_{29}$ template (see *SI Appendix*, Fig. S28 for the Pd-centered nanosystem). With the controllable synthetic procedure (combining the in situ synthesis and metal-exchange
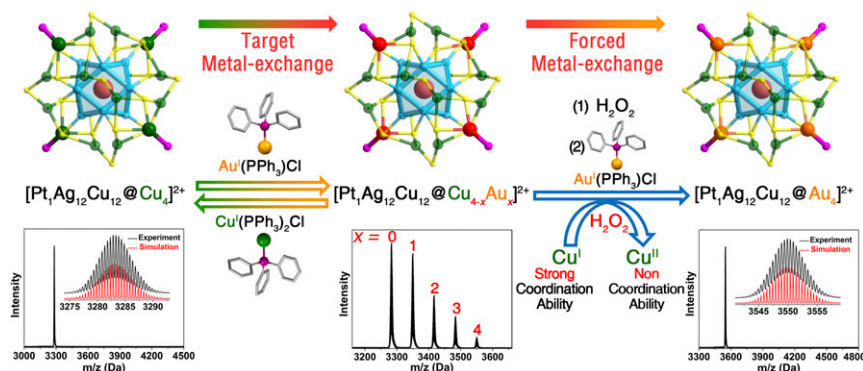
Fig. 4. M$_{29}$ nanoclusters from trimetallic to tetrametallic. Illustration of the synthetic procedures from $Pt_1Ag_{12}Cu_{16}$ to poly-dispersed $Pt_1Ag_{12}Cu_{16-x}Au_x$ ($x = $ 0–4), and then to monodispersed $Pt_1Ag_{12}Cu_{12}Au_4$ nanocluster. The blue curve represents the oxidation from Cu(I) to Cu(II) effected by H_2O_2, thus the non-coordinate ability of Cu(II) leads to the monodispersity of the final tetrametallic $Pt_1Ag_{12}Cu_{12}Au_4$ nanocluster. Color codes: cerulean sphere, Ag; pink sphere, Pt; orange sphere, Au; green sphere, Cu; red sphere, mixed Au/Cu; yellow sphere, S; purple sphere, P. For clarity, the carbon and hydrogen atoms are not shown.

Kang et al.

www.manaraa.com

method), the monometallic Ag_{29} has been precisely alloyed to bimetallic Pt_1Ag_{28}, trimetallic $Pt_1Ag_{12}Cu_{16}$, and tetrametallic $Pt_1Ag_{12}Cu_{12}Au_4$ nanoclusters (*SI Appendix*, Fig. S27A). *SI Appendix*, Fig. S27B shows the structural anatomy of the $Pt_1Ag_{12}Cu_{12}Au_4$ nanocluster. Specifically, the single Pt atom occupies the innermost position and is further enclosed by 12 Ag atoms, constituting the Pt_1Ag_{12} kernel. Then, four 3-fold symmetric $Cu_3(S\text{-}Adm)_6$ staple motifs wrap up the Pt_1Ag_{12} kernel. Because these $Cu_3(S\text{-}Adm)_6$ motifs connect each other by sharing the end thiolates, a cage-like $Cu_{12}(SR)_{18}$ is formed. Finally, 4 vertex Au-PPh_3 units block the bare corners and the whole structure is constructed, formulated $Pt_1Ag_{12}Cu_{12}Au_4(S\text{-}Adm)_{18}(PPh_3)_4$ with a tetra-stratified configuration—Pt(center)@Ag_{12}(first shell)@$Cu_{12}(S\text{-}Adm)_{18}$(second shell)@$(Ag\text{-}PPh_3)_4$(vertex).

According to the aforementioned nanocluster methodology (including the in situ synthesis, targeted metal-exchange, and forced metal-exchange methods), a library of 21 species of M_{29} (M = Ag/Cu/Pt/Pd/Au) nanoclusters has been successfully constructed. The "in situ synthesis" guarantees the single-metal occupation of the kernel, the first shell, and the second shell. Besides, a combination of "targeted metal-exchange" and "forced metal-exchange" methods guarantees the single-metal occupation of the vertex. *SI Appendix*, Fig. S29 generalizes the ESI-MS spectra and metal arrangements of these nanoclusters. ESI-MS results demonstrated the monodispersity of each nanocluster, which is of significance for the subsequent investigation on metal synergistic effect at the atomic level. The monodispersity of each nanocluster was also verified by the elemental analysis and the inductively coupled plasma-atomic emission spectrometry results of these M_{29} nanoclusters (*SI Appendix*, Tables S1 and S2). The NMR result of the M_{29} nanoclusters (here we tested Pt_1Ag_{28}, Au_1Ag_{28}, and $Pt_1Ag_{12}Cu_{16}$ nanoclusters that had been crystallized) presented only one ^{31}P peak, demonstrating the same chemical environment of the 4 PPh_3 ligands as well as the symmetry of the nanocluster's configuration (*SI Appendix*, Fig. S30).

Seven subsystems have been established on the basis of the different metal arrangement, including $Ag_{25}@M_4$, $Au_1Ag_{24}@M_4$, $Pt_1Ag_{24}@M_4$, $Pd_1Ag_{24}@M_4$, $Au_1Ag_{12}Cu_{12}@M_4$, $Pt_1Ag_{12}Cu_{12}@M_4$, and $Pd_1Ag_{12}Cu_{12}@M_4$ subsystems. Each subsystem has the same M_1(center)@M_{12}(first shell)@$M_{12}(SR)_{18}$(second shell) metal configuration. For each subsystem, 3 different types of metals could be arranged (i.e., Ag, Cu, or Au) on the vertex sites, giving rise to 3 different nanocluster members in each subsystem (*SI Appendix*, Figs. S31–S37). Accordingly, altogether 21 nanoclusters ($7 \times 3 = 21$) with monodispersity have been obtained for the M_{29} library. Evidenced by the mass spectra, the nanocluster's overall charge is "+3" when the kernel position is occupied by Ag or Au, whereas the charge is "+2" when Pt or Pd is at the innermost of the nanocluster (*SI Appendix*, Figs. S30–S37).

Synergy Effect on the Nanocluster Properties. The intermetallic synergism has been experimentally and theoretically investigated based on alloy nanoclusters, and has been proved to be the decisive effect that influences the chemical and physical properties of nanoclusters (e.g., optical, catalytic, electrochemical properties, and stability) (24–26, 30, 32–34, 45–49). The available M_{29} nanosystem now allows us to evaluate the synergistic effects in detail. Here we focus on the synergistic effects on the electronic structure of nanoclusters, and optical absorption, photoluminescence (PL), and stability.

First of all, we find that each nanocluster in the M_{29} system possesses the 8e free-electronic structure. In this context, a comparison of the oxidation states of metals in different M_{29} nanoclusters can help us infer the synergistic effects on electronic structures of these nanoclusters. *SI Appendix*, Figs. S38–S40 present the XPS results of different M_{29} nanoclusters. From the XPS results, the substitution of Ag atoms in the second shell or vertex

positions by Cu leads to the concentration of free valence electrons to the cluster's kernel, and thus the XPS peaks of inner metals shift to the M(0) peak. Collectively, owing to the differences of the metal electronegativity, substituting the parent shell metal (Ag) with more active metal (Cu) would make the free electrons less bound to the outermost shell and concentrating to the kernel. Thus, the kernel metals would tend to present a metallic state (i.e., M^0), and the shell metals will be in a more oxidized state (i.e., $M^{\delta+}$).

SI Appendix, Figs. S41–S44 present the optical absorption and PL of the 21 nanoclusters, sorted by the metal occupation of the kernel. Some important structure-optical absorption correlations have been mapped out: 1) For the kernel, substituting the central Ag atom by a Pd heteroatom hardly changes the optical absorption, whereas doping a Pt/Au heteroatom into the kernel significantly red-shifts the absorption; 2) for the second shell, exchanging the $Ag_{12}(SR)_{18}$ into $Cu_{12}(SR)_{18}$ blue-shifts the optical absorption while maintaining their initial profiles; 3) for the vertex, the characteristic absorption profiles are almost retained when the vertex Ag atoms are substituted by Cu; by contrast, metal exchanging of these vertex atoms into Au not only red-shifts the initial absorption but also generates a new peak at the range of higher wavelength.

Interestingly, all nanoclusters in the M_{29} nanosystem fluoresce when illuminated at 445 nm (*SI Appendix*, Figs. S41–S44). By comparing these PL spectra, synergy effects on PL characteristics in terms of PL intensity and emission wavelength are analyzed (Fig. 5 and *SI Appendix*, Figs. S45–S48). For the kernel, doping a Pd heteroatom into the center of M_{29} weakens the PL intensity and blue-shifts the emission; on the contrary, enhanced PL intensity as well as red-shifted emission has been observed by substituting the center Ag with a Pt or Au atom (*SI Appendix*, Fig. S45). For the second shell, alloying the $Ag_{12}(SR)_{18}$ shell into $Cu_{12}(SR)_{18}$ blue-shifts the emission wavelength and slightly reduces the PL intensity (*SI Appendix*, Fig. S46). For the vertex, substituting the vertex Ag atoms by Au cannot only red-shift the emission but also significantly enhance the PL intensity; opposite phenomena have been observed in exchanging the vertex Ag atoms with Cu (*SI Appendix*, Fig. S47). According to the above observations, the $Au_1@Ag_{12}@Ag_{12}(SR)_{18}@(Au\text{-}PPh_3)_4$ displays the highest PL intensity and maximum emission wavelength (with quantum yield of 11.6% and emission of 715 nm) among the 21 nanoclusters (Figs. 5 and 6). Collectively, based on the abovementioned correlations between the metal arrangement in the M_{29} template and PL properties, we find that controlling the
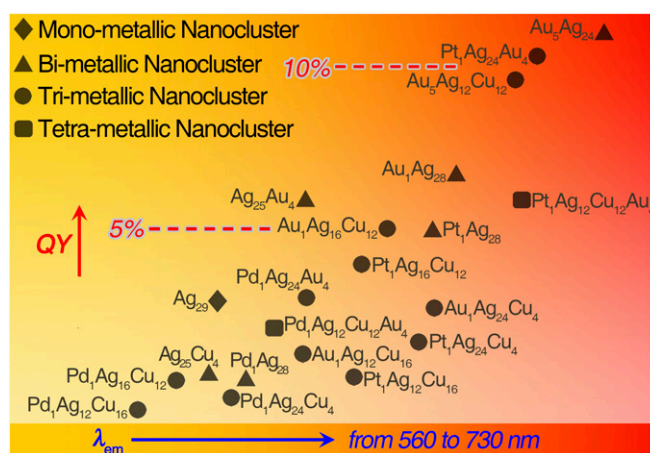

Fig. 5. Comparison of PL property of the M_{29} nanoclusters. The rhomboid, triangular, circular, and square symbols represent the mono-, bi-, tri-, and tetrametallic nanoclusters, respectively.
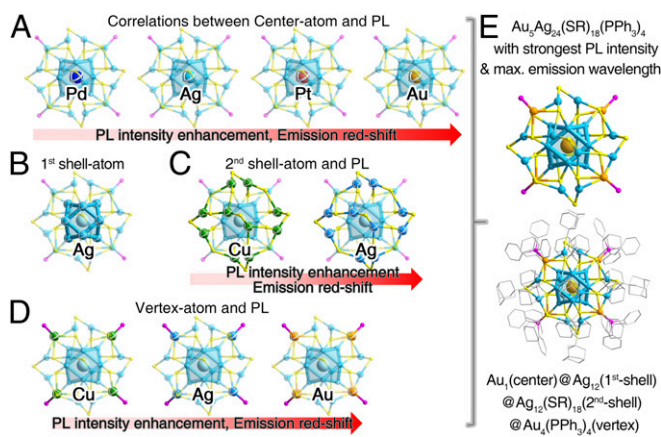
www.manaraa.com

Fig. 6. (A–D) Illustration of the strategies to enhance the PL intensity of the M_{29} nanocluster. (E) $Au_5Ag_{24}(SR)_{18}(PPh_3)_4$ nanocluster with the strongest PL intensity and the maximum emission wavelength, among these 21 nanoclusters of M_{29}.

nanocluster kernel or vertex metals with large electron affinity [note: metal electron affinity subsequence Au(2.309) > Pt(2.128) > Ag(1.302) > Cu(1.228) > Pd(0.562)] is in favor of preparing emissive nanoclusters with higher PL intensity. The obtained general trends of PL with different doping modes will provide guidelines for future work on fluorescent alloy nanoclusters.

Synergy effects on the thermal stability of these nanoclusters have also been investigated (*SI Appendix*, Figs. S48–S53). Time-dependent optical absorption of these nanoclusters (dissolved in CH_2Cl_2) was monitored at room temperature (*SI Appendix*, Figs. S48–S51). By comparing the variation trends of the absorptions, we conclude that 1) for the kernel, the stability sequence is $Pd_1M_{28} < Ag_1M_{28} < Au_1M_{28} \sim Pt_1M_{28}$; 2) for the second shell, alloying the $Ag_{12}(SR)_{18}$ shell into $Cu_{12}(SR)_{18}$ enhances the stability of nanoclusters; and 3) for the vertex, the stability sequence is $M_{25}Cu_4 > M_{25}Ag_4 \gg M_{25}Au_4$ (*SI Appendix*, Figs. S52 and S53). The correlations between the metal occupation in vertex and the stability of nanoclusters agree with the energy changes of nanoclusters derived from the DFT calculations (*SI Appendix*, Fig. S3).

Conclusion

We have developed a methodology to prepare atomically precise alloy nanoclusters based on the $M_{29}(S\text{-}Adm)_{18}(PPh_3)_4$ template (M = Au/Ag/Pd/Pt/Cu) with a tetra-stratified configuration— $M_1(center)@M_{12}(first shell)@M_{12}(SR)_{18}(second shell)@(M\text{-}PPh_3)_4(vertex)$. Owing to the easy maneuverability of each site in this M_{29} template, a library of 21 nanoclusters with atomic monodispersity has been synthesized by exploiting the in situ synthesis, targeted metal-exchange, and forced metal-exchange methods, and these nanoclusters range from monometallic to bi-, tri-, and tetrametallic constitutions. The monodispersity of each nanocluster has been verified by the ESI-MS measurement. In addition, the precise structures of these M_{29} nanoclusters enable us to uncover the intermetallic synergy at the atomic level, which provides guidelines for future work on alloy nanoclusters. Overall, the M_{29} nanosystem presented in this work is of significance not only because it provides a platform to generate alloyed nanoclusters with multimetallic compositions and monodispersed dopants but also it offers atomic-level insight into the intermetallic synergy.

Methods

Synthesis of the Monometallic $[Ag_{29}(S\text{-}Adm)_{18}(PPh_3)_4]^{3+}$. For the nanocluster synthesis, $AgNO_3$ (30 mg, 0.18 mmol) was dissolved in CH_3OH (5 mL) and $CH_3COOC_2H_5$ (35 mL) with sonication. The solution was vigorously stirred

(~1,200 rpm) with magnetic stirring for 15 min. Then, Adm-SH (0.1 g) and PPh_3 (0.1 g) were added and the reaction was vigorously stirred (~1,200 rpm) for another 90 min. After that, $NaBH_4$ (1 mL) aqueous solution (20 mg·mL^{-1}) was added quickly to the above mixture. The reaction was allowed to proceed for 36 h under a N_2 atmosphere. After that, the aqueous layer was removed, and the mixture in the organic phase was rotavaporated under vacuum. Then ~15 × 3 mL of CH_3OH was used to wash the synthesized nanoclusters. The precipitate was dissolved in CH_2Cl_2, which produced the $[Ag_{29}(S\text{-}Adm)_{18}(PPh_3)_4]^{3+}$ nanocluster. The yield is 16% based on the Ag element (calculated from the $AgNO_3$).

Synthesis of the Bimetallic $[Pt_1Ag_{28}(S\text{-}Adm)_{18}(PPh_3)_4]^{2+}$. Specifically, the metal source for synthesizing $[Ag_{29}(S\text{-}Adm)_{18}(PPh_3)_4]^{3+}$ nanocluster (i.e., $AgNO_3$, 0.18 mmol) was altered to Ag/Pt mixture ($AgNO_3/H_2PtCl_6\cdot6H_2O$ = 0.17/0.01 mmol in the $[Pt_1Ag_{28}(S\text{-}Adm)_{18}(PPh_3)_4]^{2+}$ synthesis) and the other conditions were not changed, then the $[Pt_1Ag_{28}(S\text{-}Adm)_{18}(PPh_3)_4]^{2+}$ nanoclusters were obtained. The yield is 45% based on the Ag element (calculated from the $AgNO_3$).

Synthesis of Trimetallic $[Pt_1Ag_{12+x}Cu_{16-x}(S\text{-}Adm)_{18}(PPh_3)_4]^{2+}$ ($x = 0\text{–}4$). Specifically, the metal source for synthesizing $[Ag_{29}(S\text{-}Adm)_{18}(PPh_3)_4]^{3+}$ nanocluster (i.e., $AgNO_3$, 0.18 mmol) was altered to Ag/Cu/Pt mixture ($AgNO_3/Cu^I(PPh_3)_2Cl/H_2PtCl_6\cdot6H_2O$ = 0.1/0.07/0.01 mmol in the $[Pt_1Ag_{12+x}Cu_{16-x}(S\text{-}Adm)_{18}(PPh_3)_4]^{2+}$ synthesis) and the other conditions were not changed, then the $[Pt_1Ag_{12+x}Cu_{16-x}(S\text{-}Adm)_{18}(PPh_3)_4]^{2+}$ nanoclusters were obtained. The yield is 15% based on the Ag element (calculated from the $AgNO_3$).

Synthesis of Trimetallic $[Pt_1Ag_{12}Cu_{16}(S\text{-}Adm)_{18}(PPh_3)_4]^{2+}$ and $[Pt_1Ag_{16}Cu_{12}(S\text{-}Adm)_{18}(PPh_3)_4]^{2+}$. A target metal-exchange method was exploited to "focus" the polydispersed $[Pt_1Ag_{12+x}Cu_{16-x}(S\text{-}Adm)_{18}(PPh_3)_4]^{2+}$ ($x = 0\text{–}4$) nanoclusters into the $[Pt_1Ag_{12}Cu_{16}(S\text{-}Adm)_{18}(PPh_3)_4]^{2+}$ or $[Pt_1Ag_{16}Cu_{12}(S\text{-}Adm)_{18}(PPh_3)_4]^{2+}$. Specifically, 0.1 mmol $[Pt_1Ag_{12+x}Cu_{16-x}(S\text{-}Adm)_{18}(PPh_3)_4]^{2+}$ was dissolved in 20 mL CH_2Cl_2; 1 mmol $Cu^I(PPh_3)_2Cl$ was added to the above solution and the solution was further vigorously stirred (~1,200 rpm) for 30 min. The organic phase was rotavaporated under vacuum and washed several times with CH_3OH. The precipitate was dissolved in CH_2Cl_2, which produced pure $[Pt_1Ag_{12}Cu_{16}(S\text{-}Adm)_{18}(PPh_3)_4]^{2+}$. The yield is 80% based on the $[Pt_1Ag_{12+x}Cu_{16-x}(S\text{-}Adm)_{18}(PPh_3)_4]^{2+}$ nanoclusters. Changing the $Cu^I(PPh_3)$ Cl into the $Ag^I(PPh_3)NO_3$ generated pure $[Pt_1Ag_{16}Cu_{12}(S\text{-}Adm)_{18}(PPh_3)_4]^{2+}$ with a 70% yield.

Synthesis of Tetrametallic $[Pt_1Ag_{12}Cu_{16-x}Au_x(S\text{-}Adm)_{18}(PPh_3)_4]^{2+}$ ($x = 0\text{–}4$). A "target metal-exchange" method was exploited to alloy the trimetallic $[Pt_1Ag_{12}Cu_{16}(S\text{-}Adm)_{18}(PPh_3)_4]^{2+}$ into the tetrametallic $[Pt_1Ag_{12}Cu_{16-x}Au_x(S\text{-}Adm)_{18}(PPh_3)_4]^{2+}$ ($x = 0\text{–}4$) nanoclusters. Specifically, 0.1 mmol $[Pt_1Ag_{12}Cu_{16}(S\text{-}Adm)_{18}(PPh_3)_4]^{2+}$ was dissolved in 20 mL CH_2Cl_2; 0.5 mmol $Au^I(PPh_3)Cl$ was added to the above solution and the solution was further vigorously stirred (~1,200 rpm) for 60 min. The organic phase was rotavaporated under vacuum. The precipitate was dissolved in CH_2Cl_2, which produced the tetrametallic $[Pt_1Ag_{12}Cu_{16-x}Au_x(S\text{-}Adm)_{18}(PPh_3)_4]^{2+}$ nanocluster. The yield is 85% based on the $[Pt_1Ag_{12}Cu_{16}(S\text{-}Adm)_{18}(PPh_3)_4]^{2+}$.

Synthesis of Tetrametallic $[Pt_1Ag_{12}Cu_{12}Au_4(S\text{-}Adm)_{18}(PPh_3)_4]^{2+}$. The "forced metal-exchange" method was exploited to alloy the polydispersed $[Pt_1Ag_{12}Cu_{16-x}Au_x(S\text{-}Adm)_{18}(PPh_3)_4]^{2+}$ ($x = 0\text{–}4$) nanoclusters into the mono-dispersed $[Pt_1Ag_{12}Cu_{12}Au_4(S\text{-}Adm)_{18}(PPh_3)_4]^{2+}$ nanocluster. Specifically, 0.1 mmol $[Pt_1Ag_{12}Cu_{16-x}Au_x(S\text{-}Adm)_{18}(PPh_3)_4]^{2+}$ was dissolved in 20 mL CH_2Cl_2; 200 μL H_2O_2 was added and the solution was further vigorously stirred (~1,200 rpm) for 3 min. Then, 0.5 mmol $Au^I(PPh_3)Cl$ was added to the above solution and further vigorously stirred for 30 min. The $H_2O_2@Au^I(PPh_3)Cl$ addition was repeated 3 times to eliminate the Cu^I coordination completely. The organic phase was then precipitated with a large amount of CH_3OH. Finally, the precipitate was dissolved in CH_2Cl_2, which produced the monodispersed $[Pt_1Ag_{12}Cu_{16}Au_4(S\text{-}Adm)_{18}(PPh_3)_4]^{2+}$ nanocluster. The yield is 20% based on the $[Pt_1Ag_{12}Cu_{16-x}Au_x(S\text{-}Adm)_{18}(PPh_3)_4]^{2+}$.

Crystallization of $Au_1Ag_{28}(S\text{-}Adm)_{18}(PPh_3)_4$ and $Pt_1Ag_{12}Cu_{16}(S\text{-}Adm)_{18}(PPh_3)_4$. Single crystals of $Au_1Ag_{28}(S\text{-}Adm)_{18}(PPh_3)_4$ and $Pt_1Ag_{12}Cu_{16}(S\text{-}Adm)_{18}(PPh_3)_4$ nanoclusters were grown at room temperature for 7 d in CH_2Cl_2/CH_3OH. Then, red crystals were collected and the structures of $Au_1Ag_{28}(S\text{-}Adm)_{18}(PPh_3)_4$ and $Pt_1Ag_{12}Cu_{16}(S\text{-}Adm)_{18}(PPh_3)_4$ were determined by X-ray crystallography.

Other than the nanoclusters in the Pt-centered system, details of synthesis of other cases are provided in *SI Appendix*.

1. P. C. Chen et al., Polyelemental nanoparticle libraries. *Science* **352**, 1565–1569 (2016).
2. K. D. Gilroy, A. Ruditskiy, H. C. Peng, D. Qin, Y. Xia, Bimetallic nanocrystals: Syntheses, properties, and applications. *Chem. Rev.* **116**, 10414–10472 (2016).
3. M. A. Zeb Gul Sial, M. A. Ud Din, X. Wang, Multimetallic nanosheets: Synthesis and applications in fuel cells. *Chem. Soc. Rev.* **47**, 6175–6200 (2018).
4. S. Wang et al., Shuttling single metal atom into and out of a metal nanoparticle. *Nat. Commun.* **8**, 848 (2017).
5. J. L. Fenton, B. C. Steimle, R. E. Schaak, Tunable intraparticle frameworks for creating complex heterostructured nanoparticle libraries. *Science* **360**, 513–517 (2018).
6. R. Jin, C. Zeng, M. Zhou, Y. Chen, Atomically precise colloidal metal nanoclusters and nanoparticles: Fundamentals and opportunities. *Chem. Rev.* **116**, 10346–10413 (2016).
7. I. Chakraborty, T. Pradeep, Atomically precise clusters of noble metals: Emerging link between atoms and nanoparticles. *Chem. Rev.* **117**, 8208–8271 (2017).
8. P. Liu, R. Qin, G. Fu, N. Zheng, Surface coordination chemistry of metal nanomaterials. *J. Am. Chem. Soc.* **139**, 2122–2131 (2017).
9. M. van der Linden et al., Single Au atom doping of silver nanoclusters. *ACS Nano* **12**, 12751–12760 (2018).
10. T. Higaki et al., Anomalous phonon relaxation in $Au_{333}(SR)_{79}$ nanoparticles with nascent plasmons. *Proc. Natl. Acad. Sci. U.S.A.* **116**, 13215–13220 (2019).
11. M. Zhou et al., Three-orders-of-magnitude variation of carrier lifetimes with crystal phase of gold nanoclusters. *Science* **364**, 279–282 (2019).
12. M. Agrachev, M. Ruzzi, A. Venzo, F. Maran, Nuclear and electron magnetic resonance spectroscopies of atomically precise gold nanoclusters. *Acc. Chem. Res.* **52**, 44–52 (2019).
13. A. W. Cook, T. W. Hayton, Case studies in nanocluster synthesis and characterization: Challenges and opportunities. *Acc. Chem. Res.* **51**, 2456–2464 (2018).
14. Q. Yao, X. Yuan, T. Chen, D. T. Leong, J. Xie, Engineering functional metal materials at the atomic level. *Adv. Mater.* **30**, e1802751 (2018).
15. B. Bhattarai et al., Chemistry and structure of silver molecular nanoparticles. *Acc. Chem. Res.* **51**, 3104–3113 (2018).
16. K. Kwak, D. Lee, Electrochemistry of atomically precise metal nanoclusters. *Acc. Chem. Res.* **52**, 12–22 (2019).
17. B. Nieto-Ortega, T. Bürgi, Vibrational properties of thiolate-protected gold nanoclusters. *Acc. Chem. Res.* **51**, 2811–2819 (2018).
18. K. L. D. M. Weerawardene, H. Häkkinen, C. M. Aikens, Connections between theory and experiment for gold and silver nanoclusters. *Annu. Rev. Phys. Chem.* **69**, 205–229 (2018).
19. T. Zhao, P. J. Herbert, H. Zheng, K. L. Knappenberger, Jr, State-resolved metal nanoparticle dynamics viewed through the combined lenses of ultrafast and magneto-optical spectroscopies. *Acc. Chem. Res.* **51**, 1433–1442 (2018).
20. X. Kang, M. Zhu, Tailoring the photoluminescence of atomically precise nanoclusters. *Chem. Soc. Rev.* **48**, 2422–2457 (2019).
21. S. Kenzler, C. Schrenk, A. Schnepf, $Au_{108}S_{24}(PPh_3)_{16}$: A highly symmetric nanoscale gold cluster confirms the general concept of metalloid clusters. *Angew. Chem. Int. Ed. Engl.* **56**, 393–396 (2017).
22. T. Sugiuchi, Y. Shichibu, K. Konishi, An inherently chiral Au_{24} framework with double-helical hexagold strands. *Angew. Chem. Int. Ed. Engl.* **57**, 7855–7859 (2018).
23. W. Chen, S. Chen, Oxygen electroreduction catalyzed by gold nanoclusters: Strong core size effects. *Angew. Chem. Int. Ed. Engl.* **48**, 4386–4389 (2009).
24. K. Kwak et al., A molecule-like $PtAu_{24}(SC_6H_{13})_{18}$ nanocluster as an electrocatalyst for hydrogen production. *Nat. Commun.* **8**, 14723 (2017).
25. S. Xie, H. Tsunoyama, W. Kurashige, Y. Negishi, T. Tsukuda, Enhancement in aerobic alcohol oxidation catalysis of Au_{25} clusters by single Pd atom doping. *ACS Catal.* **2**, 1519–1523 (2012).
26. M. S. Bootharaju, C. P. Joshi, M. R. Parida, O. F. Mohammed, O. M. Bakr, Templated atom-precise galvanic synthesis and structure elucidation of a $[Ag_{24}Au(SR)_{18}]^-$ nanocluster. *Angew. Chem. Int. Ed. Engl.* **55**, 922–926 (2016).
27. T. Udayabhaskararao et al., Ag_7Au_6: A 13-atom alloy quantum cluster. *Angew. Chem. Int. Ed. Engl.* **51**, 2155–2159 (2012).
28. W. T. Chang et al., Eight-electron silver and mixed gold/silver nanoclusters stabilized by selenium donor ligands. *Angew. Chem. Int. Ed. Engl.* **56**, 10178–10182 (2017).
29. Z. Lei, X. L. Pei, Z. J. Guan, Q. M. Wang, Full protection of intensely luminescent gold(I)-silver(I) cluster by phosphine ligands and inorganic anions. *Angew. Chem. Int. Ed. Engl.* **56**, 7117–7120 (2017).
30. S. Wang et al., A 200-fold quantum yield boost in the photoluminescence of silver-doped $Ag_{(x)}Au_{(25-x)}$ nanoclusters: The 13th silver atom matters. *Angew. Chem. Int. Ed.* **53**, 2376–2380 (2014).
31. Y. Wang et al., Atomically precise alkynyl-protected metal nanoclusters as a model catalyst: Observation of promoting effect of surface ligands on catalysis by metal nanoparticles. *J. Am. Chem. Soc.* **138**, 3278–3281 (2016).
32. K. Kim et al., Elucidating the doping effect on the electronic structure of thiolate-protected silver superatoms by photoelectron spectroscopy. *Angew. Chem. Int. Ed. Engl.* **58**, 11637–11641 (2019).
33. S. Hossain et al., Alloy clusters: Precise synthesis and mixing effects. *Acc. Chem. Res.* **51**, 3114–3124 (2018).
34. Z. Gan, N. Xia, Z. Wu, Discovery, mechanism, and application of antigalvanic reaction. *Acc. Chem. Res.* **51**, 2774–2783 (2018).
35. S. Wang et al., Metal exchange method using Au_{25} nanoclusters as templates for alloy nanoclusters with atomic precision. *J. Am. Chem. Soc.* **137**, 4018–4021 (2015).
36. S. Sharma et al., Tuning the electronic structure of thiolate-protected 25-atom clusters by co-substitution with metals having different preferential sites. *Dalton Trans.* **45**, 18064–18068 (2016).
37. C. Kumara, C. M. Aikens, A. Dass, X-ray crystal structure and theoretical analysis of $Au_{25-x}Ag_x(SCH_2CH_2Ph)_{18}^-$ alloy. *J. Phys. Chem. Lett.* **5**, 461–466 (2014).
38. E. Gottlieb, H. Qian, R. Jin, Atomic-level alloying and de-alloying in doped gold nanoparticles. *Chemistry* **19**, 4238–4243 (2013).
39. H. Qian et al., Monoplatinum doping of gold nanoclusters and catalytic application. *J. Am. Chem. Soc.* **134**, 16159–16162 (2012).
40. M. A. Tofanelli, T. W. Ni, B. D. Phillips, C. J. Ackerson, Crystal structure of the $PdAu_{24}(SR)_{18}^0$ superatom. *Inorg. Chem.* **55**, 999–1001 (2016).
41. X. Kang et al., The tetrahedral structure and luminescence properties of Bi-metallic $Pt_1Ag_{28}(SR)_{18}(PPh_3)_4$ nanocluster. *Chem. Sci.* **8**, 2581–2587 (2017).
42. J. Yan et al., Asymmetric synthesis of chiral vimetallic $[Ag_{28}Cu_{12}(SR)_{24}]^{4-}$ nanoclusters via ion pairing. *J. Am. Chem. Soc.* **138**, 12751–12754 (2016).
43. H. Yang et al., Structural evolution of atomically precise thiolated bimetallic $[Au(12+n)Cu_{32}(SR)(30+n)]^{4-}$ (n = 0, 2, 4, 6) nanoclusters. *J. Am. Chem. Soc.* **136**, 7197–7200 (2014).
44. X. K. Wan et al., Atomically precise bimetallic $Au_{19}Cu_{30}$ nanocluster with an icosidodecahedral Cu_{30} shell and an alkynyl-Cu interface. *J. Am. Chem. Soc.* **139**, 9451–9454 (2017).
45. X. Kang, L. Xiong, S. Wang, Y. Pei, M. Zhu, Combining the single-atom engineering and ligand-exchange strategies: Obtaining the single-heteroatom-doped $Au_{16}Ag_1$ (S-Adm)$_{13}$ nanocluster with atomically precise structure. *Inorg. Chem.* **57**, 335–342 (2018).
46. M. S. Bootharaju, L. Sinatra, O. M. Bakr, Distinct metal-exchange pathways of doped Ag_{25} nanoclusters. *Nanoscale* **8**, 17333–17339 (2016).
47. K. R. Krishnadas, A. Baksi, A. Ghosh, G. Natarajan, T. Pradeep, Structure-conserving spontaneous transformations between nanoparticles. *Nat. Commun.* **7**, 13447 (2016).
48. N. Yan et al., Bimetal doping in nanoclusters: Synergistic or counteractive? *Chem. Mater.* **28**, 8240–8247 (2016).
49. K. L. D. M. Weerawardene, C. M. Aikens, Origin of photoluminescence of $Ag_{25}(SR)_{18}^-$ nanoparticles: Ligand and doping effect. *J. Phys. Chem. C* **122**, 2440–2447 (2018).

www.manaraa.com